# Experimental Observation of Self-Organised Mode-Locked Emission in a W-Band Free-Electron Maser

H. S. Marks[a], M. Khorosh[b]

[a] Lancaster University, School of Engineering, England, United Kingdom
[b] Ariel University, Department of Engineering, Ariel 40700, Israel

## Abstract

Experimental observation is reported of passive, self-organised mode-locking in a high-power free-electron maser (FEM) oscillator operating near 103 GHz, using a ~1.36 MeV, 1.15 A energy-recovered electron beam. Macropulses of 10 μs duration were recorded in which mode-locking is established from the onset of measurable radiation and persists throughout the pulse. Power-detector and heterodyne measurements show a regular train of kW-level spikes with a spacing of 10.4 ns, consistent with the cavity free spectral range. A modal analysis of the intermediate-frequency signal reveals strong phase coherence across more than sixteen longitudinal modes. A distinct sideband appears with a spacing that remains stable to within 0.2 MHz even though the carrier frequency drifts by several megahertz between pulses due to variations in beam energy. This behaviour contradicts the power-dependent scaling expected from synchrotron-driven FEL sidebands and instead indicates a cavity-anchored coupling mechanism. The results demonstrate that robust passive mode-locking can arise naturally in mm-wave FEM oscillators without external modulation.

***Index Terms*—FEL Oscillator, Mode-Locking, Free Electron Maser, Carrier-Modulation.**

## 1. Introduction

Free electron masers and lasers (FEM/FEL) are a class of vacuum electronic device that can produce coherent and directed electromagnetic radiation from mm-waves to X-rays. They work by forcing the transfer of energy from a relativistic electron beam to a radiation field. Relativistic electrons are directed into an undulator, a sinusoidal arrangement of a magnetic or electric field (most commonly a static magnetic field) [1]. This work is concerned with an FEM operating with a continuous electron beam with energy close to 1.36 MeV, in an oscillator configuration. A resonator sits within the undulator, and a proportion of the radiation generated is reflected back from an outcoupling mirror and contained within the resonator [2].

The gain curve of an FEM/FEL will cover a frequency range related to the beam energy and system parameters. Within this range an oscillator enforces the condition that only certain discrete frequencies can oscillate without high loss, these are the longitudinal modes. Any mode can grow if the multiple of gain ($G$) and roundtrip reflectivity ($R_{rt}(f)$) is greater than one, $GR_{rt} > 1$. Competition exists between these possible modes. Factors which influence a single-frequency outcome include both the gain profile and roundtrip-reflectivity, which is a function of frequency. A weak external signal can be injected into the cavity to bias mode competition and accelerate the rise of a particular longitudinal mode [3, 4], which is useful when a single carrier frequency and narrow bandwidth are desirable, such as for high-capacity mm-wave links [5, 6].

Conversely, it is possible to bias the mode competition such that many longitudinal modes can co-exist. This produces a periodic train of spikes of wideband radiation. This is called Mode-Locking and is a well-known phenomenon widely explored in the optical domain [7, 8]. Less commonly it has been

demonstrated in a variety of vacuum electronic devices in the microwave and millimetre-wave bands. Mode-Locking is critical for metrology, time-keeping, and ultra-fast imaging, where a regular train of narrow (but broadband) pulses is essential [9]. In the mm-wave/THz domain this can be used for fault detection and imaging [10].

Alberti et al. reported generation of mode-locked pulses around 260.5 GHz by Q-switching the cavity. Rapid intracavity power swings generate sidebands that support multi-mode operation. Spikes of 1.2 ns width were measured with a 4.2 ns repetition rate and peak power of ~5 W [11]. The limited sideband structure generated by the modulation constrains the extent of achievable mode locking.

Traveling-wave tubes (TWTs) are broadband amplifiers that operate with a slow-wave structure [12]. Ginzburg et al. recently showed that a gyro-TWT operating with two beams, one of which acts as a saturable absorber, can be used to produce mode-locked output. Pulses in the Ka-band (26–40 GHz) with FWHM ≈ 0.4 ns, peak intensity ~100 kW, and a repetition rate of 2.5 ns were measured [13]. In the W-band, Rozental et al. simulated a TWT using a feedback delay [14]. Numerical modelling predicts sub-nanosecond pulse formation; the authors note that in practice an additional amplifier could increase the available output power.

In Free Electron Masers, Jerby and Bekefi demonstrated mode-locking at 8–11 GHz with a period of 37 ns and a micro-pulse width of 5 ns using a quasi-CW 250 A beam at 250 keV [15]. A PIN-diode modulator was inserted into the ring cavity, controlling transmission (amplitude modulation) with a period equal to the cavity roundtrip time (power inferred < 2 kW). Backward-wave interactions have been explored in certain low-energy (~45 keV), dispersion-engineered free-electron devices employing periodically loaded slow-wave structures, where they can influence gain and spectral structure [16]. Savilov et al. modelled mode-locking behaviour in a klystron-like FEM using a small-signal injection region for modulation before the undulator [17]. The theory of mode-locking in FELs has been previously described [18, 19].

Collectively, these demonstrations rely on active modulation or engineered nonlinearities. In contrast, passive self-organized mode-locking in high-power mm-wave FEL/FEM oscillators remains comparatively unexplored and experimentally under-documented. In the present work, passive coupling of the longitudinal modes enables continuous mode-locked operation without active modulation, secondary electron beams, or intra-cavity PIN diodes.

Ottaviani et al. [20] described the simulated formation of ‘frozen spikes’ in deeply saturated FEL oscillators in terms of sideband instability and super-mode coupling. A behaviour that is physically equivalent to passive mode-locking. However, in our case the locking frequency remains fixed independent of intra-cavity power, indicating a distinct beam-mediated inter-mode coupling mechanism rather than the synchrotron oscillation driven sideband process commonly described in FEL simulations. While the theoretical literature on FEL-oscillator mode-locking is extensive, there are comparatively few time-resolved experimental measurements. The present work provides direct observations of the spectral and temporal evolution of the oscillator during the onset of locking and throughout a steady-state train of spikes until the beam is switched off.

# 2. Experimental Setup

An energy recovery electrostatic accelerator was used to supply the ~1.36 MeV electron beam. The 1.15 A beam was derived from capacitors which are trickle charged by a 50 kV supply. The overall setup is shown in Fig. 1. The electron beam generated from the thermionic cathode transfers only a small fraction of its kinetic energy in the interaction region; simulations for similar conditions indicate an

average energy decrease of order ~45 keV [21], with a broadened post-interaction energy distribution (some electrons gain energy while the majority lose). Then the electrons are decelerated such that they are collected at low energy. This means the majority of the electron energy is recovered and a distinction should be made between the electronic efficiency and the overall system efficiency.

There are eight controllable focusing elements before the undulator: four focusing coils in the low-energy injector region and four quadrupoles after electrostatic acceleration to ~1.36 MeV. In addition, steering elements are used to maintain beam alignment, and the acceleration line itself provides some focusing. In the present setup, imperfect electron collection leads to a gradual discharge of the high-voltage terminal during operation, resulting in a beam-energy decrease at a rate of approximately 1 kV/μs. This behaviour is not inherent to Van de Graaff accelerators, but reflects practical engineering constraints of the present system. The resulting slow energy drift causes modest frequency pulling of the longitudinal modes, but does not significantly affect the stability of masing or mode-locking over the ~10 μs pulse duration. To mitigate this effect, a voltage-ramping device (VRD) is connected to the undulator and resonator. When the VRD is employed the resonator is electrically isolated from the high-voltage terminal, and its potential can be ramped relative to the terminal during the pulse, increasing the electron kinetic energy upon entry to the undulator. By appropriate choice of ramp rate, this allows partial or complete compensation of the terminal voltage droop, or deliberate over-compensation when required. After leaving the resonator, the electron beam is decelerated back to the terminal potential. The VRD waveform is set to begin after a user-defined delay, and the ramped voltage is discharged after a further user-defined interval, returning the resonator potential to its pre-ramped state. The microwave power extracted during masing is supplied by the relatively low-voltage, high-current systems; ideally, no significant energy is drawn from the high-voltage terminal itself. Further details of the VRD operation are given in earlier work [21, 22].

The undulator is a planar Halbach type with 26 periods of 44.4 mm, composed of SmCo bar magnets [23]. The resonator main interaction region which sits within the undulator is an 890 mm waveguide with two corrugated and two smooth walls. The corrugations are on the walls in the plane of the electron oscillations, with overall waveguide width 15 mm, and height 10.7 mm, the corrugations have depth 0.75 mm, and period 0.8 mm. The corrugated interaction waveguide supports the fundamental $HE_{11}$ eigenmode with smooth transmission across the operating band and does not introduce mode conversion. Two additional sections form the ends of the resonator and decouple the electron beam from the microwaves. The electrons enter the resonator via a flat rectangular window which is fixed to the end of a smooth-walled 25 mm wide by 10.7 mm high waveguide of length 210 mm. At the other end of the corrugated waveguide a second smooth-walled section is connected, likewise with dimensions 25mm width, and 10.7 mm height. Electrons exit the resonator through a hole in a parabolic mirror 208 mm from the junction with the corrugated waveguide. The parabolic mirror reflects the masing radiation up out of the electron-beam line to a second parabolic mirror arranged in a confocal configuration. The radiation is then reflected to a series of wire-grids which control the out-coupling of the radiation. When the fundamental $HE_{11}$ mode diffracts into the wider smooth-walled section, splitting and subsequent recombination of the radiation enable effective de-coupling of the electron beam and the microwave field [24, 25]. The specific resonator configuration and testing is described in detail in a prior work [26]. The total optical length of the resonator is 1.514 m. The cathode to collector distance is 13.48 meters, table I details the main system specifications.

A transmission line consisting of cylindrical corrugated waveguides transports the masing power to a user room. Power and frequency are sampled using a mixer (Quinstar QMB-FB BB W) and a power

detector (Millitech DXP-10 RPFW0). An HP sweep oscillator (86290B) is set to constant frequency out and used in combination with a Millitech 380 AMC 10-RFH00 A16800 for the Local Oscillator. The signals have been recorded on a Keysight DSCX3104A 5 GS/s, 1 GHz bandwidth oscilloscope.

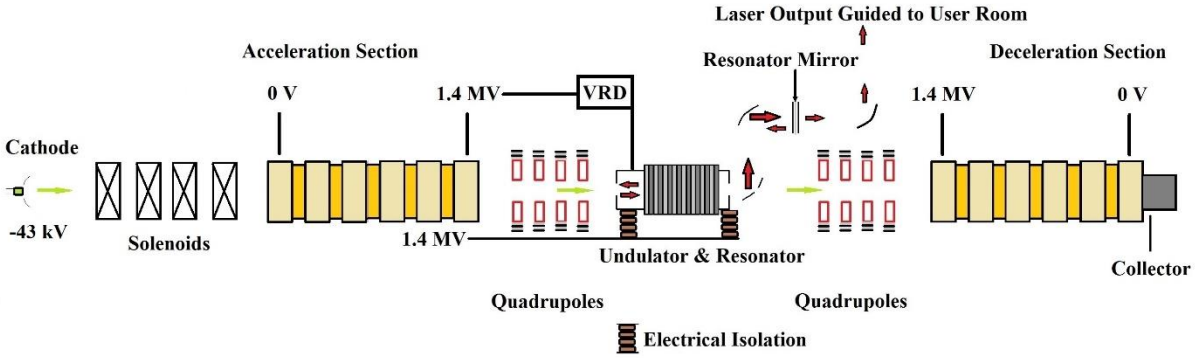


Fig. 1. Schematic of the EA-FEM based on a Tandem Van-der-Graaf generator. The electrons are generated using a thermionic cathode. They are focused and then injected into an acceleration section, which is located within a high-pressure tank where they are brought to near the speed of light. Beyond this, they are focused with quadrupoles into the undulator and resonator combination to generate maser radiation. Beyond this they are re-focused and decelerated.

TABLE I: PROPERTIES OF THE EA-FEL

| | |
|---|---|
| Beam Current | 1-2 A |
| Beam Energy | 1.35-1.45 MeV |
| Undulator Period | $\lambda_U = 44.4\ mm$ |
| Undulator Periods | $N_U = 24$ |
| Undulator field Amplitude | $0.193\ T$ |
| Waveguide Fundamental Mode | $HE_{11}$ |
| Radiation Frequency | 95-110 GHz |

## 3. Results

Figure 2 shows the detected power profile of a 10 µs self-mode-locked pulse centred near 103 GHz. Mode-locked spikes appear from the very start of the measurable signal and persist for the full pulse duration. The shape of the macropulse reflects the evolving electron beam energy. Up to 3.8 µs the terminal voltage decreases at ~0.98 kV/µs, causing a gradual reduction in power. At 3.8 µs an 18 kV voltage ramp is applied to the beam, producing an intra-pulse increase in electronic efficiency and a corresponding rise in power. The ramp is discharged at 7.8 µs, after which the power decreases again. These changes in power are driven by the beam-energy evolution and are independent of the mode-locking mechanism. A shorter segment from 0–3.6 µs is shown in Fig. 3, where the periodic structure is more clearly resolved. This regular train of spikes arises from a fixed-phase relation between many simultaneously excited longitudinal modes.

To show the modal behaviour in the time domain a spectrogram was generated from the Intermediate Frequency (IF), see Fig. 4. The Local Oscillator (LO) was set to 102.498 GHz. Clearly many modes are in simultaneous masing throughout the pulse. There are modes above and below the LO, the modes below the LO are folded onto the positive x-axis. Modes above and below the LO can be distinguished by their spacing and the direction the frequency is pulled when the accelerating potential goes down or up. To consider the relative weight of the modes a Fast Fourier Transform (FFT) of the IF is plotted in Fig. 5. In addition to the longitudinal modes, sidebands can be observed due to the Amplitude Modulation of the modes. Figure 6 shows a narrower time slice of the power measurement. The mean period over 727 successive spikes is 10.32 ns, with a standard deviation of

0.1 ns. The apparent full width at half maximum (FWHM) of the spikes is 1.4 ± 0.2 ns as measured by the power detector; this width is limited by the temporal response of the detection system.

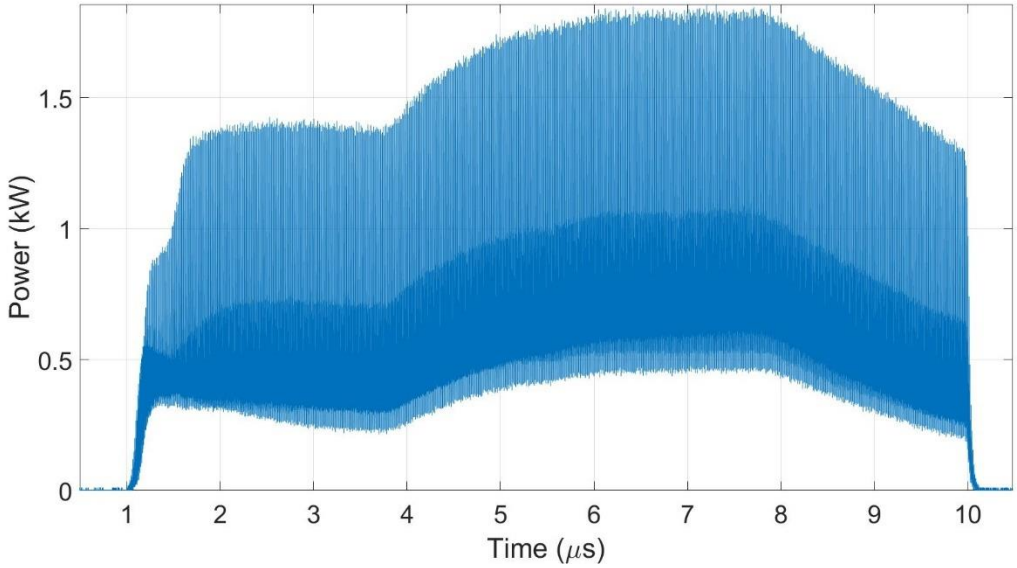


Fig 2: Power as a function of time showing self-mode-locking for the complete pulse. As is typical with this system the accelerating potential of the High-Voltage-Terminal (HVT) dropped at ~-0.98 kV/µs. At 3.8 µs an 18 kV ramp in the beam energy with a rise time of 0.63 µs is started, it's discharged at 7.8 µs. The terminal voltage was initially ~1.32 MV (above the -43 kV of the cathode region) and the cathode current 1.15 A.

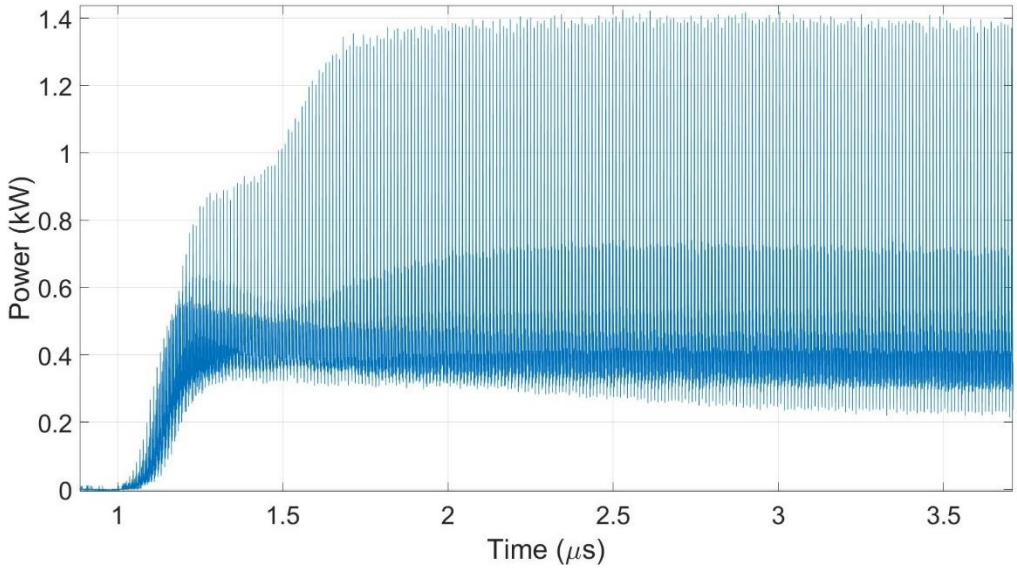


Fig 3: Power as a function of time showing self-mode-locking for the first 3.5 $\mu s$ of a 10 $\mu s$ pulse. During this time the beam energy is falling at ~-0.98 kV/µs.

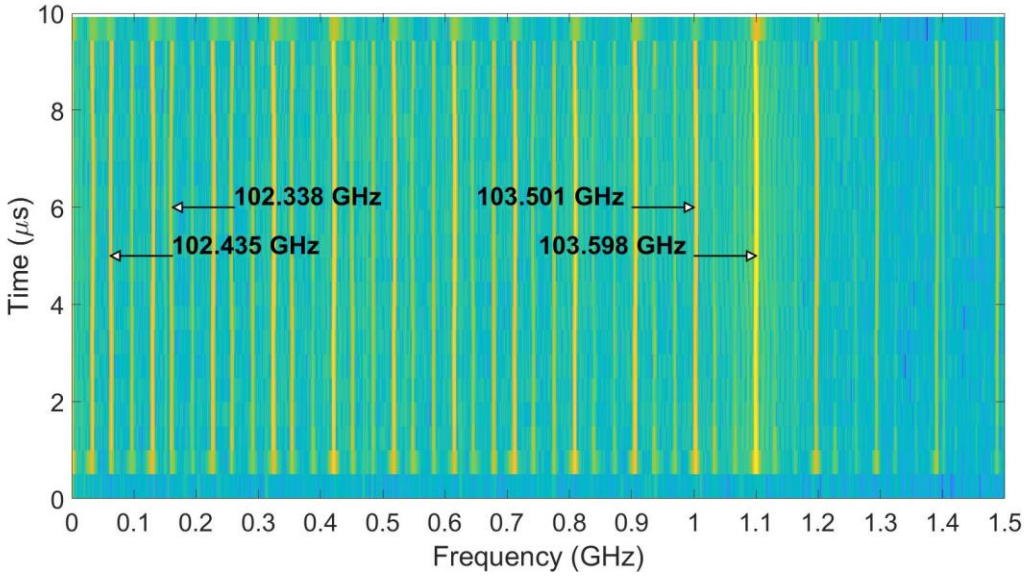


Fig 4: Spectrogram of the IF of the pulse shown in Fig. 2. The Local Oscillator was set to 102.498 GHz. Free Spectral Range (FSR) ~96.43 MHz.

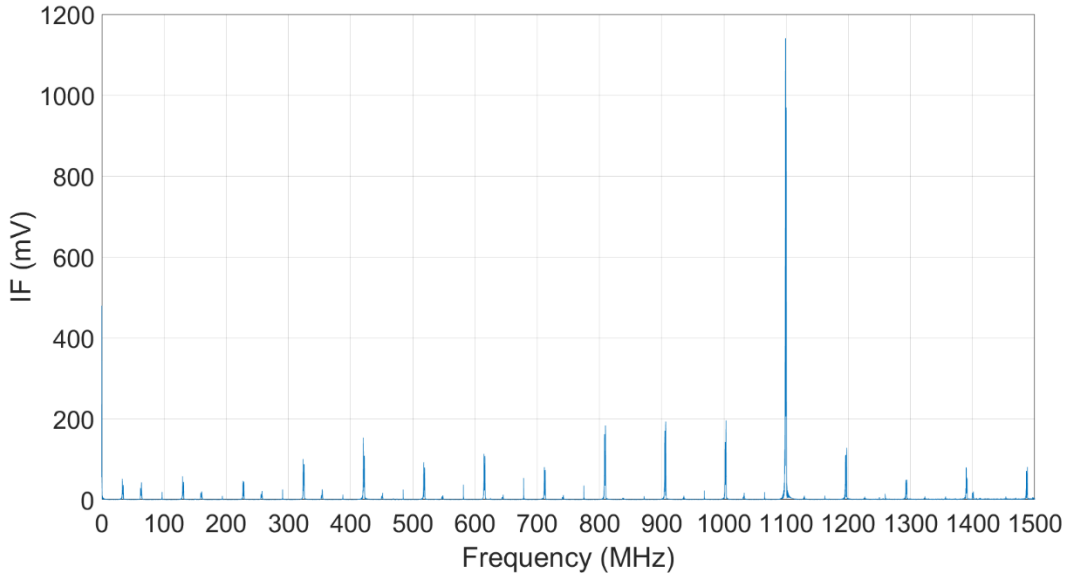


Fig 5: Intermediate Frequency (IF) as a function of frequency for the pulse shown in Fig. 2. The Local Oscillator (LO) is set to 102.498 GHz. Longitudinal modes above and below the LO are shown along the same positive axis. The spacing of the longitudinal modes is 96.9 MHz. Between these longitudinal modes we also observe sidebands due to the amplitude modulation of these modes.

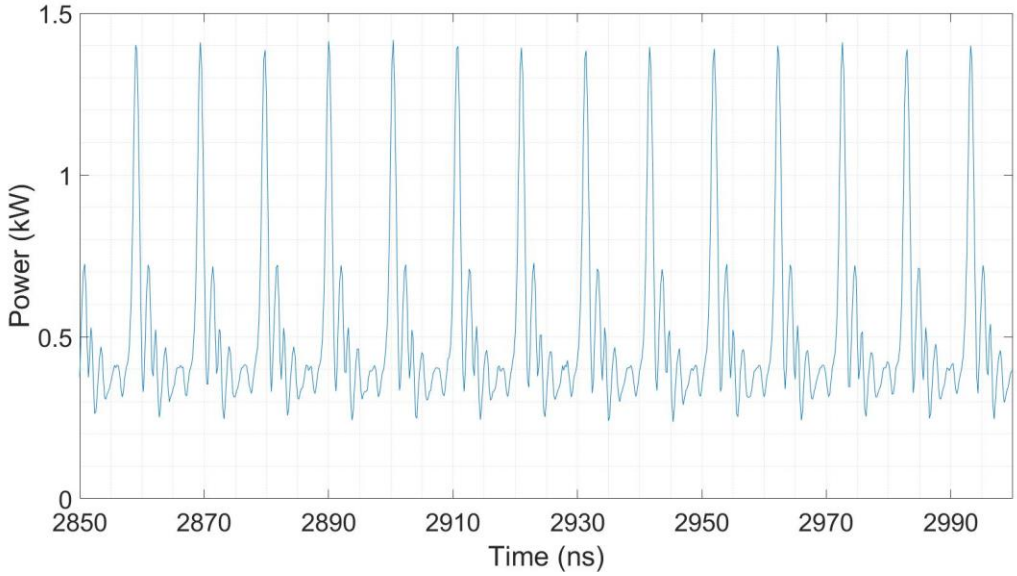


Fig 6: Zooming in on a shorter time slice of Fig. 3 to show the broadband spikes in power. The spacing between these peaks is on average 10.32 ns, which corresponds to a frequency of 96.9 MHz. The FWHM of the peaks as measured with the power detector is 1.4 ± 0.2 ns.

*3.1 Phase Coherence*

Using the intermediate-frequency signal $V_{IF}(t)$, the relative phase evolution $\Delta\phi_m(t)$ of each longitudinal mode *m* was extracted with respect to the dominant mode (by power) at 103.597 GHz. For each mode the complex envelope was obtained numerically by mixing $V_{IF}(t)$ with $e^{-i\omega_m t}$ followed by low-pass filtering. $\Delta\phi_m(t)$ was then defined as the difference between the instantaneous phase of mode $m$ and that of the reference mode. Over the interval 2-9 µs, seven of the strongest modes exhibit a mean absolute phase deviation $\langle | \Delta\phi_m(t) | \rangle < 6.2°$. Across the full set of detected modes between 102.144 GHz and 103.694 GHz, $\langle | \Delta\phi_m(t) | \rangle$ lies in the range 2.2°–18.8°. This confirms strong phase coherence among the dominant longitudinal modes throughout the macropulse and is consistent with stable passive mode-locking.

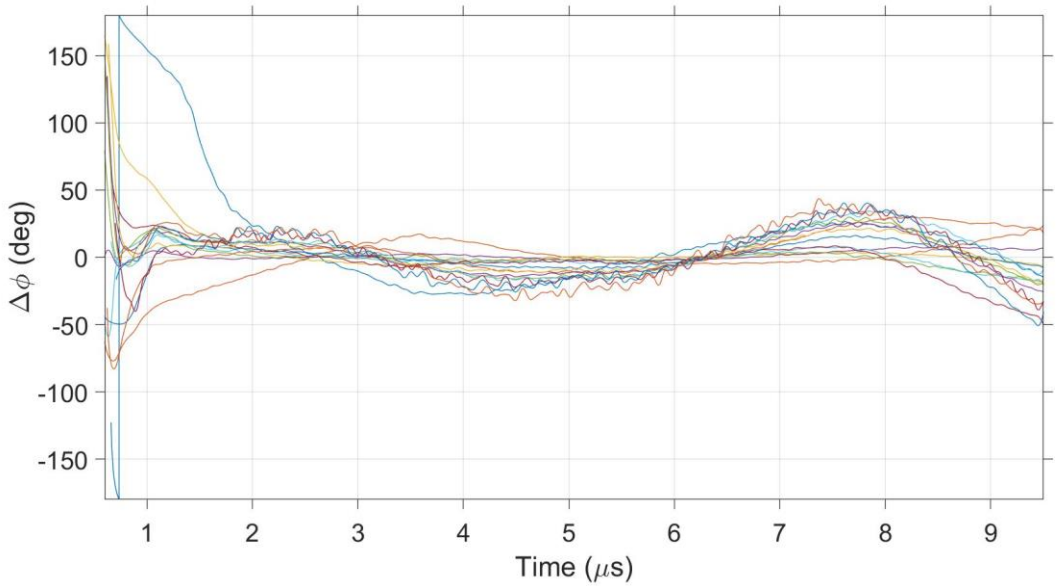


Figure 7: Longitudinal mode phase coherence relative to the dominant mode at 103.597 GHz. Upper freq. range 103.694 GHz Lower freq. range 102.144 GHz.

*3.2 Sidebands*

To examine the sideband behaviour, Fig. 8 shows the FFTs of six independent mode-locked pulses, each centred on a longitudinal mode and its lower sideband. Two features are immediately apparent. First, the carrier frequency (one of the longitudinal modes) shifts by several megahertz between pulses, reflecting the pulse-to-pulse variation in beam energy. Second, despite this carrier drift, the sideband frequencies remain fixed to within 0.2 MHz across all six pulses. The sidebands are therefore referenced to the laboratory frame rather than to the instantaneous resonant frequency of the beam. Although the relative sideband amplitudes vary both between and within pulses, their absolute frequencies remain essentially constant. This behaviour is consistent with a stable, cavity-defined mode-locking frequency that is insensitive to small changes in beam energy.

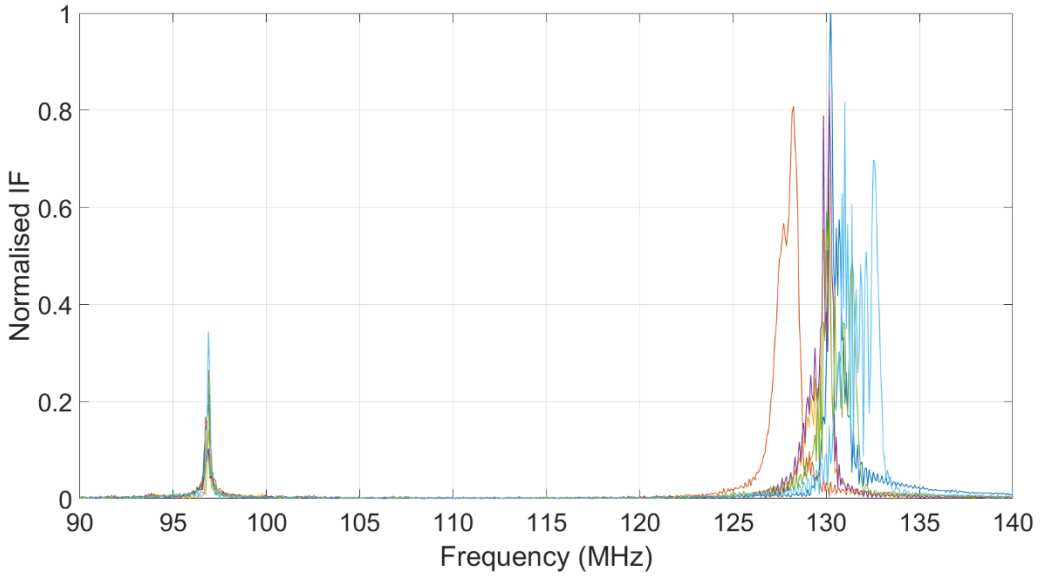


Figure 8: Observing the overlaid FFT of six pulses focused in on a mode ~130 MHz from the LO at 102.498 GHz For each of the six pulses there is a corresponding lower sideband.

# 4. Discussion

*4.1 Interpretting the Sideband Behaviour*

In this system in the steady single-mode regime sidebands have not previously been noted. This is consistent with the absence of significant amplitude modulation (AM). In the mode-locked regime, however, the radiation field is a phase-locked sum of adjacent longitudinal modes and forms a pulse-like envelope that circulates in the cavity. This envelope acts as an effective ponderomotive potential supermode. In addition to the standing-wave field of the dominant longitudinal mode. In FEL theory, trapped electrons oscillating in the ponderomotive potential can produce AM at the synchrotron frequency Ωs, which depends on the radiation power and beam energy. Sidebands generated in this way are expected to shift as the intra-cavity power and synchronism conditions change. In our measurements, by contrast, the carrier frequency (a longitudinal mode) shifts by several megahertz within and between pulses in response to small variations in beam energy, while the sideband frequencies remain fixed to within 0.2 MHz across all six pulses shown in Fig. 8. Including in a pulse where the output power changes by ~50% during the macropulse. This behaviour rules out a simple synchrotron-oscillation origin for the observed sidebands. Instead, the sideband frequencies are effectively defined in the laboratory frame by the cavity dynamics of the mode-locked field (for example via a parasitic higher-order mode path). They appear insensitive to changes in beam energy or output power. Such cavity-anchored sidebands are consistent with a stable passive mode-locking mechanism that is not governed by the space-charge-driven sideband processes commonly assumed in FEL simulations.

The experimental evidence instead points to a mechanism anchored by the cavity rather than the beam frame. A lab-fixed spectral offset of ~31–34 MHz corresponds to an effective coupling delay of 29–33 ns, suggesting a fixed-path secondary feedback channel within the resonator system. The precise origin of this delayed coupling is beyond the scope of the present work, but possibilities include weak excitation of a higher-order resonator mode, unbalanced mode conversion or imperfect recombination in the resonator decoupling sections or a small fraction of radiation returning via a

longer external path. Such pathways naturally generate a stable beating with the longitudinal mode comb, producing a passive and power-insensitive sideband spacing consistent with the observations.

*4.2 Periodic Spikes in Power, General Consideration*

The FWHM of the spikes shown in Fig. 6 are limited by the response time of the detector. In free electron maser/laser oscillators the shortest achievable spike duration is limited by optical–electron slippage in the undulator. For the present undulator the slippage time is $\tau_{slip} \approx 0.15$ ns, implying a minimum spike width of order $2\tau_{slip} \approx 0.3$ ns. The corresponding Fourier-limited spectral width (~5 GHz) represents an upper bound on the bandwidth of modes that can coherently participate in the mode-locked pulse. In practice, the number of contributing modes is further constrained by the frequency-dependent cavity reflectivity and gain profile.

The 1.4 ± 0.2 ns FWHM spikes measured by the power detector reflects not the intrinsic pulse width but the instrument response; the actual field spikes are likely much narrower. The measured modal spectra in Fig. 5 show $> 16$ identifiable longitudinal modes. This is consistent with a multi-gigahertz bandwidth and with spike envelopes substantially compressed relative to the detector-limited trace.

Overall, the temporal structure is consistent with passive mode-locking sustained by a broad, phase-coherent set of longitudinal modes rather than by power-dependent dynamical effects. The persistence of well-formed spikes throughout the 10 μs macropulse suggests that the coupling mechanism stabilising the phases remains effective even as the beam energy and output power vary significantly during the pulse.

## 5. Conclusion:

This work has experimentally demonstrated passive, self-organised mode-locking in a high-power free-electron maser oscillator operating near 103 GHz. A train of temporally regular spikes persists for the full 10 μs macropulse and is supported by strong phase coherence across more than sixteen longitudinal modes. The measured sideband spacing remains fixed to within 0.2 MHz even as the carrier frequency shifts by several megahertz, indicating that the locking frequency is defined by cavity dynamics rather than beam-dependent synchrotron processes. Together, these results show that stable passive mode-locking can arise naturally from the resonator's internal coupling, without external modulation, and over a wide range of beam conditions. Further work will examine the origin of the effective coupling path responsible for the observed cavity-anchored sideband structure.

[1] D.A. Deacon, L.R. Elias, J.M. Madey, G.J. Ramian, H.A. Schwettman and T.I. Smith, 1977. First operation of a free-electron laser. Physical Review Letters, 38(16), p.892. DOI: https://doi.org/10.1103/PhysRevLett.38.892
[2] H.S. Marks, A. Gover, D. Borodin, A. Damti, M. Kanter, Y. Lasser, M. Einat, Y. Vashdi, Y. Lurie and A. Friedman, Radiation power out-coupling optimization of a free electron laser oscillator. IEEE Transactions on Microwave Theory and Techniques, 64(3), pp.1006-1014, 2016. DOI: 10.1109/TMTT.2016.2516532
[3] G. Ramian, S. Takahashi and M. Sherwin, The UCSB MM-FEL Injection Locking System, Proceedings of FEL Novosibirsk, Russia, 2007.
[4] M. Cohen, et al., "Masing and Single-Mode Locking in a Free-Electron Maser," Phys. Rev. Lett. 74, 3812–3815 (1995). DOI: https://doi.org/10.1103/PhysRevLett.74.3812
[5] R.C. Daniels, & R.W. Heath, "60 GHz wireless communications: Emerging requirements and design recommendations," IEEE Veh. Technol. Mag. 2(3), 41–50 (2007). DOI: 10.1109/MVT.2008.915320

[6] T. Kürner & S. Priebe, “Towards THz communications—status in research, standardization and regulation,” J. Infrared Milli. Terahz Waves 35, 53–62, (2014). https://doi.org/10.1007/s10762-013-0014-3
[7] A. Yariv, “Introduction to Optoelectronics”, SBN: 03-084694-3, Holt, Rinehart and Winston, Inc.
[8] H.A. Haus, 2002. Mode-locking of lasers. IEEE Journal of Selected Topics in Quantum Electronics, 6(6), pp.1173-1185.
[9] T.W. Hänsch, “Nobel Lecture: Passion for precision,” Rev. Mod. Phys. 78, 1297–1309 (2006).
[10] H. Zhong, J. Xu, X. Xie, T. Yuan, R. Reightler, E. Madaras and X.C. Zhang, Nondestructive defect identification with terahertz time-of-flight tomography. IEEE sensors journal, 5(2), pp.203-208, 2005.
[11] S. Alberti, et al., Nanosecond Pulses in a THz Gyrotron Oscillator Operating in a Mode-Locked Self-Consistent Q-Switch Regime, Phys. Rev. Lett. 111, 205101, (2013).
[12] Claudio Paoloni, Diana Gamzina, Rosa Letizia, Yuan Zheng & Neville C. Luhmann Jr. (2021) Millimeter wave traveling wave tubes for the 21st Century, Journal of Electromagnetic Waves and Applications, 35:5, 567-603, DOI: 10.1080/09205071.2020.1848643
[13] N.S. Ginzburg et al., Ka-Band 100-kW Subnanosecond Pulse Generator Mode-Locked by Cyclotron Resonance Absorber, Phys. Rev. Applied 16, 054045 (2021).
[14] R.M. Rozental, A.A. Ivanov, D.A. Sidorov, and M.N. Vilkov. Self-mode-locking operation regimes in a TWT with low-level delayed feedback. *IEEE Transactions on Electron Devices*, *70*(11), pp.5940-5945, , 2023.
[15] E. Jerby and G. Bekefi, AM mode-locking of a free-electron laser oscillator. IEEE journal of quantum electronics, 29(11), pp.2845-2851, 1993.
[16] C. Balfour, The design of a backward wave free electron laser (Doctoral dissertation, University of Liverpool) 1996.
[17] A.V. Savilov, N.Y. Peskov, and V.N. Philippov, Spatiotemporal dynamics of a free electron maser oscillator with broadband feedback and klystronlike interaction region. *Physical Review Special Topics—Accelerators and Beams*, *8*(8), p.080702, 2005.
[18] P.J. Van Der Slot and H.P. Freund, Three-dimensional, time-dependent analysis of high-and low-q free-electron laser oscillators. Applied Sciences, 11(11), p.4978, 2021.
[19] G. Dattoli, L. Mezi, A. Renieri, and A. Torre, Free-electron laser saturated regime, cavity modulation, and harmonic generation. *IEEE journal of quantum electronics*, *34*(9), pp.1782-1789, 2002.
[20] P.L. Ottaviani, S. Pagnutti, G. Dattoli, E. Sabia, V. Petrillo, P.J.M. Van Der Slot, S. Biedron, and S. Milton, Deep saturated Free Electron Laser oscillators and frozen spikes. *Nuclear Instruments and Methods in Physics Research Section A: Accelerators, Spectrometers, Detectors and Associated Equipment*, *834*, pp.108-117, 2016.
[21] H.S. Marks, Y. Lurie, E. Dyunin, and A. Gover, Enhancing electron beam radiative energy extraction efficiency in free-electron laser oscillators through beam energy ramping. IEEE Transactions on Microwave Theory and Techniques, 65(11), pp.4218-4224, 2017.
[22] H.S. Marks, D. Borodin, and Y. Lurie, Power and spectral evolution of a Free Electron Laser oscillator with electron beam energy ramping. *Nuclear Instruments and Methods in Physics Research Section A: Accelerators, Spectrometers, Detectors and Associated Equipment*, *1004*, p.165376, 2021.
[23] H. S. Marks et al., “Wiggler improvement based on single axis magnetic measurement, synthesized 3-D field simulation of trajectories and sorting of lateral focusing magnets,” Nuclear Instrum. Methods Phys. Res. Section A, Accelerators, Spectrometers, Detectors, Associated Equipment, vol. 660, no. 1, pp. 15–21, 2011.
[24] L. A. Rivlin and A. T. Semenov, “Transmission of images through optical-waveguides,” Laser Focus, vol. 17, no. 2, p. 82, Feb. 1981.
[25] N. L. Aleksandrov, A. V. Chirkov, G. G. Denisov, and S. V. Kuzikov, “Mode content analysis from intensity measurements in a few cross sections of oversized waveguides,” Int. J. Infrar. Millimeter Waves, vol. 18, no. 6, pp. 1323–1334, 1997.
[26] H.S. Marks, and A. Gover, Talbot effect mm-wave resonator for an electrostatic accelerator free electron laser. IEEE Transactions on Microwave Theory and Techniques, 66(1), pp.3-10, 2017.